



Article

An Improved UAV-Based ATI Method Incorporating Solar Radiation for Farm-Scale Bare Soil Moisture Measurement

Renhao Jia^{1,2}, Jianli Liu^{1,3}, Jiabao Zhang¹, Yujie Niu^{1,2}, Yifei Jiang^{1,2}, Kefan Xuan^{1,2} , Can Wang^{1,2}, Jingchun Ji^{1,2} , Bin Ma^{4,5,6} and Xiaopeng Li^{1,*}

- ¹ Institute of Soil Science, Chinese Academy of Sciences, Nanjing 210008, China; jia renhao@issas.ac.cn (R.J.); jlliu@issas.ac.cn (J.L.); niuyujie@issas.ac.cn (Y.N.); jyf@issas.ac.cn (Y.J.); kfxuan@issas.ac.cn (K.X.); wangcan@issas.ac.cn (C.W.); jcji@issas.ac.cn (J.J.)
- ² University of Chinese Academy of Sciences, Beijing 100049, China
- ³ University of Chinese Academy of Sciences, Nanjing 211135, China
- ⁴ Institute of Soil and Water Resources and Environmental Science, College of Environmental and Resource Sciences, Zhejiang University, Hangzhou 310058, China; bma@zju.edu.cn
- ⁵ Zhejiang Provincial Key Laboratory of Agricultural, Resources and Environment, Zhejiang University, Hangzhou 310058, China
- ⁶ ZJU-Hangzhou Global Scientific and Technological Innovation Center, Zhejiang University, Hangzhou 310058, China
- * Correspondence: lixp@issas.ac.cn

Abstract: The use of UAV-based remote sensing for soil moisture has developed rapidly in recent decades, with advantages such as high spatial resolution, flexible work arrangement, and ease of operation. In bare and low-vegetation-covered soils, the apparent thermal inertia (ATI) method, which adopts thermal infrared data from UAV-based remote sensing, has been widely used for soil moisture estimation at the field scale. However, the ATI method may not perform well under inconsistent weather conditions due to inconsistency of the intensity of the soil surface energy input. In this study, an improvement of the ATI method (ATI-R), considering the variation in soil surface energy input, was developed by the incorporation of solar radiation measurements. The performances of the two methods were compared using field experiment data during multiple heating processes under various weather conditions. It showed that on consistently sunny days, both ATI-R and ATI methods obtained good correlations with the volumetric water contents (VWC) ($R^2_{ATI-R} = 0.775$, $RMSE_{ATI-R} = 0.023 \text{ cm}^3 \cdot \text{cm}^{-3}$ and $R^2_{ATI} = 0.778$, $RMSE_{ATI} = 0.018 \text{ cm}^3 \cdot \text{cm}^{-3}$) on cloudy or a combination of sunny and cloudy days as long as there were significant soil-heating processes despite the different energy input intensities; the ATI-R method could perform better than the ATI method (cloudy: $R^2_{ATI-R} = 0.565$, $RMSE_{ATI-R} = 0.024 \text{ cm}^3 \cdot \text{cm}^{-3}$ and $R^2_{ATI} = 0.156$, $RMSE_{ATI} = 0.033 \text{ cm}^3 \cdot \text{cm}^{-3}$; combined: $R^2_{ATI-R} = 0.673$, $RMSE_{ATI-R} = 0.028 \text{ cm}^3 \cdot \text{cm}^{-3}$ and $R^2_{ATI} = 0.310$, $RMSE_{ATI} = 0.032 \text{ cm}^3 \cdot \text{cm}^{-3}$); and on overcast days, both the ATI-R and ATI methods could not perform satisfactorily ($R^2_{ATI-R} = 0.027$, $RMSE_{ATI-R} = 0.024 \text{ cm}^3 \cdot \text{cm}^{-3}$ and $R^2_{ATI} = 0.027$, $RMSE_{ATI} = 0.031 \text{ cm}^3 \cdot \text{cm}^{-3}$). The results indicate that supplemental solar radiation data could effectively expand applications of the ATI method, especially for inconsistent weather conditions.

Keywords: soil moisture; apparent thermal inertia (ATI); solar radiation; thermal infrared; UAV-based remote sensing



Citation: Jia, R.; Liu, J.; Zhang, J.; Niu, Y.; Jiang, Y.; Xuan, K.; Wang, C.; Ji, J.; Ma, B.; Li, X. An Improved UAV-Based ATI Method Incorporating Solar Radiation for Farm-Scale Bare Soil Moisture Measurement. *Remote Sens.* **2023**, *15*, 3769. <https://doi.org/10.3390/rs15153769>

Academic Editors: Ning Li and Beril Kallfelz Sirmacek

Received: 24 May 2023

Revised: 19 July 2023

Accepted: 26 July 2023

Published: 29 July 2023



Copyright: © 2023 by the authors. Licensee MDPI, Basel, Switzerland. This article is an open access article distributed under the terms and conditions of the Creative Commons Attribution (CC BY) license (<https://creativecommons.org/licenses/by/4.0/>).

1. Introduction

Soil moisture is critical for agriculture and crop management [1,2]. In recent decades, the use of UAV-based remote sensing for soil moisture monitoring has developed rapidly due to its inherent advantages of having high spatial resolution, flexible work arrangement, and ease of operation [3–8]. Remote sensing for soil moisture monitoring mainly uses visible-near-infrared, thermal infrared, and microwave-based imaging technologies [9–15].

Visible-near-infrared methods have been widely applied; however, they may be easily affected by vegetation and surface roughness, which could lead to unstable monitoring results [6,16]. Microwave methods have better penetration capability than visible-near-infrared methods; however, the equipment is usually large and is challenging to carry by mini UAVs, being more suitable for manned aircraft and satellite-based remote sensing [15,17–19]. In contrast, thermal infrared cameras are usually light and accurate, and the relationships between soil thermal properties and soil moisture have been fully studied [20–24]; therefore, they seem more suitable for UAV-based soil moisture monitoring. However, thermal infrared-based methods are sensitive to energy inputs and could be easily affected by weather conditions [24,25]. A method to reduce the impact of inconsistent energy input on thermal infrared remote sensing during various weather conditions is the primary focus of this study.

In bare soil or sparse-vegetation-covered surface areas, the thermal inertia method is the most commonly used method for soil moisture estimation [20,22]. The thermal inertia method based on thermal infrared imagery was first proposed in the 1970s by Weston et al. [26]. Pratt improved the thermal inertia model based on application tests by considering more factors, such as thermal conductivity, solar radiance, average humidity of the surface and atmosphere, average air temperature and surface roughness [27]. The main difficulty in applying Pratt's model is that it requires numerous parameters and complex calculations; Price proposed a simplified apparent thermal inertia (ATI) index to simplify the calculation [28], and the ATI index positively correlates with soil moisture.

$$ATI = \frac{1 - \alpha}{\Delta T_d} \quad (1)$$

where α is the surface albedo (dimensionless) and ΔT_d is the diurnal (daytime and nighttime) temperature difference ($^{\circ}\text{C}$).

However, there may exist ATI index application problems, which uses the soil diurnal temperature difference and the surface albedo to characterize the proportion of energy inputted into soil [28], when the surface energy inputs vary among the sampling days [29] due to the method's simplification of the energy input. Even on clear and cloudless days, which are recommended conditions for the application of the ATI method [30], the actual solar radiation intensities still vary significantly, which then introduces inaccuracy into the soil moisture measurements. For multi-process soil moisture measurements, the ΔT_d values may be the same in different processes, but the inability to quantify solar radiation makes it impossible to determine whether the corresponding water contents are the same. Therefore, the correlation between soil moisture and the ATI index is difficult to accurately find under multiple heating processes, so the ATI method is unstable in measuring multi-process soil moisture. Palombo et al. used the ATI method to measure soil moisture by recalculating the ATI index for each sampling process and fitting the results to the current day water contents, with a resulting R^2 of approximately 0.62 [31]. This result was acceptable since it considered the diurnal variations in solar radiation, but the requirement to recalculate the ATI index each time would increase computational effort, and it would be difficult to apply the model for the current day to the next day's soil moisture measurements. In contrast, when fitting ATI indices and moisture content from different processes without considering radiation variations, the correlations between ATI indices and moisture content weakened; in some relevant studies, the R^2 fell below 0.6 [32–34].

From the perspective of soil physics, adding solar radiation measurement may be a feasible improvement to the ATI method for VWC monitoring under different solar radiation processes. Soil volumetric heat capacity is the quantity of heat that needs to be absorbed or released by the soil for every 1°C change [35]. Similarly to soil thermal inertia, soil volumetric heat capacity is also affected by moisture, resulting in different rates of soil temperature variations for the same energy input. However, the volumetric heat capacity of the soil is an explicit relationship between the amount of energy and the amount of temperature change. In contrast, the ATI replaces the actual energy with $1 - \alpha$. The surface

energy inputs are different for multiple natural heating processes. Therefore, adding solar radiation measurements to quantify the surface energy input for each process makes it clear that ΔT occurs under each energy input. Such a method can measure soil moisture for multiple processes only if the relationship between the energy input and the ΔT is clarified in the method.

The objectives of this study are to (1) propose an improved ATI method (ATI-R) incorporating the measurement of total solar radiation, (2) examine the feasibility and performance of the ATI-R method under a single heating process and multiple heating processes, and (3) compare the performance of the ATI-R and ATI methods under different weather types.

2. Materials and Methods

In this study, we proposed the ATI-R method based on the soil thermal properties, which combines the ATI index with the solar radiation measurements. The ATI-R method was evaluated and compared to the ATI method in a field moisture-controlled experiment using UAV-obtained thermal and ground-obtained total solar radiation information.

2.1. The ATI-R and ATI Methods

As a three-phase mixture of solid, liquid, and gaseous matter, soil has a volumetric heat capacity composed of the heat capacity of each phase and its corresponding proportion [36].

$$C_s = X_a C_a + X_w C_w + \sum_{j=1}^N X_{sj} C_{sj} \quad (2)$$

where X_a , X_w , and X_{sj} are the volume fractions of soil air, water, and solid-phase components, respectively, and C_a , C_w , and C_{sj} are the volumetric heat capacities of air, water, and soil solid-phase components, respectively. The relationship between soil volumetric heat capacity (C_s) and soil moisture is similar to that which exists between ATI and soil moisture and is as follows [35]:

$$C_s = \frac{Q}{V \cdot \Delta T_S} \quad (3)$$

where C_s is the soil volumetric heat capacity ($\text{J} \cdot \text{cm}^{-3} \cdot ^\circ\text{C}^{-1}$), Q is the absorbed energy (J), ΔT_S is the soil temperature difference ($^\circ\text{C}$), and V is the soil natural volume (cm^3).

C_a can usually be ignored when calculating C_s , since the volumetric heat capacity of air ($1.26 \times 10^{-3} \text{ J} \cdot \text{cm}^{-3} \cdot ^\circ\text{C}^{-1}$) is much lower than that of water ($4.18 \text{ J} \cdot \text{cm}^{-3} \cdot ^\circ\text{C}^{-1}$) and solid-phase components (approximately $1.92 \text{ J} \cdot \text{cm}^{-3} \cdot ^\circ\text{C}^{-1}$) [37]. The soil bulk density can be used instead of the volume fraction of the solid phase for calculating the soil volumetric heat capacity.

$$C_s = \theta \cdot C_w + \rho_b \cdot C_b \quad (4)$$

where θ is the soil volumetric water content ($\text{cm}^3 \cdot \text{cm}^{-3}$), ρ_b is the soil bulk density ($\text{g} \cdot \text{cm}^{-3}$), C_w is the water volumetric heat capacity ($4.18 \text{ J} \cdot \text{cm}^{-3} \cdot ^\circ\text{C}^{-1}$), and C_b is the soil solid-phase heat capacity (approximately $0.71\text{--}0.91 \text{ J} \cdot \text{g}^{-1} \cdot ^\circ\text{C}^{-1}$).

Substituting Equation (4) into Equation (3), the equation becomes:

$$\theta = \frac{Q}{V \cdot \Delta T \cdot C_w} - \frac{\rho_b \cdot C_b}{C_w} \quad (5)$$

C_w is a constant, and C_b can also be considered a constant for a specific type of soil. ρ_b varies slowly under undisturbed conditions for the same area. Therefore, ignoring the change in bulk density, the soil volumetric water content is proportional to the ratio of Q to ΔT :

$$\theta \propto \frac{Q}{\Delta T} \quad (6)$$

Substituting albedo and measurement of solar radiation intensity for Q , Equation (6) can be written as:

$$\theta \propto \frac{R_t(1 - \alpha)}{\Delta T} \quad (7)$$

where R_t is the cumulative intensity of the total solar radiation (kJ).

Based on the relationship between C_s and VWC and Equation (7), an ATI-R index is proposed and defined as:

$$\text{ATI-R} = \frac{R_t(1 - \alpha)}{\Delta T} \quad (8)$$

where R_t is the cumulative total solar radiation intensity (kJ), and ΔT is the soil temperature increment ($^{\circ}\text{C}$).

The ATI index was calculated based on Equation (1).

The following equation exists between ATI-R and VWC and ATI and VWC:

$$\text{VWC} = a_1 \times \text{ATI-R} + b_1 \ \& \ \text{VWC} = a_2 \times \text{ATI} + b_2 \quad (9)$$

2.2. Field Experiment Design

A field moisture-controlled experiment was arranged at the Fengqiu State Key Agro-Ecological Experimental Station, Chinese Academy of Sciences ($34^{\circ}53' - 35^{\circ}14' \text{N}$, $114^{\circ}14' - 114^{\circ}46' \text{E}$) in Fengqiu, Henan Province, China, in May 2022. The study area is flat, with an average elevation of 67.5 m above sea level; the primary soil type is fluvo-aquic soil, and the main cropping pattern is winter wheat–summer corn rotation. The area has a semi-arid, semi-humid temperate monsoon climate with an average annual precipitation of 615.1 mm, but precipitation resources are unevenly distributed and mainly concentrated in summer (about 45–65% of the annual precipitation).

A bare field was selected as the study area, with a flat surface without noticeable bumps and depressions. The experiment used a completely randomized design with 5 soil moisture levels and 3 replications for each level, totaling 15 plots, each with an area of 6.25 m^2 ($2.5 \text{ m} \times 2.5 \text{ m}$), with a protective row of 0.75 m width between each plot to avoid water disturbance between neighboring plots (Figure 1a). The field water-holding capacity of the experimental area was measured to be about $0.320 \text{ cm}^3 \cdot \text{cm}^{-3}$. Accordingly, we designed 5 water treatments (T0, T1, T2, T3, and T4), where T0 was the no-watering treatment, as this experiment's control check (CK). The remaining 4 treatments (T1, T2, T3, and T4) increased by 10%, 20%, 30%, and 40% of field holding capacity based on the T0 soil moisture content. The 5 watering treatments with watering amounts were 0, 3.2, 6.4, 9.6, and 12.8 mm, respectively. The VWC used for method testing was based on actual measurements of the oven-drying method.

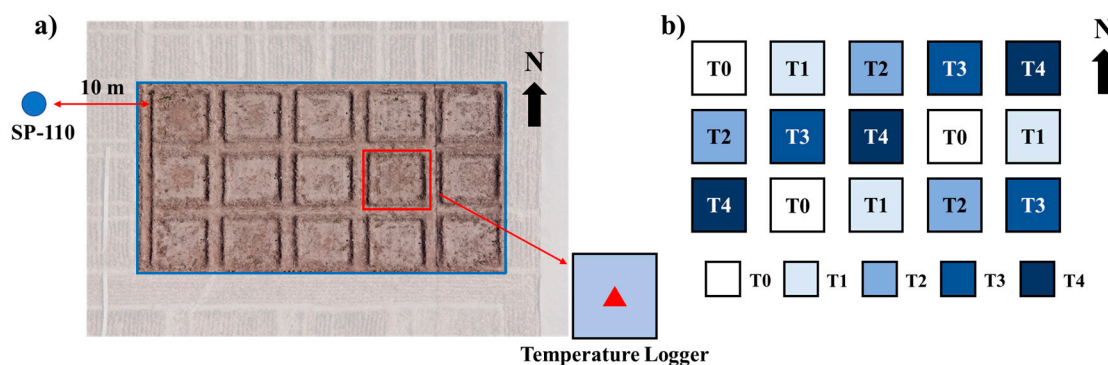


Figure 1. (a) UAV-based Vis-NIR image of the experimental area and schematic of the location of the SP-110 total radiation sensor and temperature logger, and (b) distribution image of watering treatments in each plot. T0 was no-watering treatment, as the CK. The watering amounts with T1, T2, T3, and T4 were 10% (3.2 mm), 20% (6.4 mm), 30% (9.6 mm), and 40% (12.8 mm) of the field water-holding capacity, respectively, based on the T0 soil moisture.

During May 2nd and 11th, 2022, UAV-based remote sensing images were obtained daily in the experimental plots. In addition, ground-based experimental data, including the total solar radiation intensity and the VWC measurement from the soil samples, were collected synchronously. The corresponding methods of data acquisition were as follows.

The flight altitudes of UAV-based remote sensing were all conducted at 6 m and the soil temperatures and Vis-NIR images were acquired by a thermal infrared camera (Zemuse H20T, Shenzhen, China, Figure 2b) and a multispectral camera (Rededge-MX, Micasense, Seattle, WA, USA, Figure 2c) mounted on the UAV (M300 RTK, Shenzhen, China, Figure 2a), respectively. The H20T camera operates in the 8–14 μm wavelength range, has a temperature measurement range between -40 to 150 $^{\circ}\text{C}$ (high gain mode) and -40 to 550 $^{\circ}\text{C}$ (low gain mode), and has an image resolution of 640×512 . The RedEdge-MX has 5 wavelength bands, of blue, green, red, red edge, and near-infrared, respectively, and has an image resolution of 1280×960 . Two batches of thermal infrared images were taken daily at approximately 5:30 and 14:00 local time. The times representing the lowest and highest soil surface temperatures were determined in advance by soil temperature loggers (IDEASTYLE, Suzhou, China, Figure 2d) buried 1–2 cm beneath the surface. The soil temperature increment was calculated by:

$$\Delta T = T_{1400} - T_{0530} \quad (10)$$

where T_{1400} and T_{0530} are the soil temperatures acquired by the UAV-based thermal infrared camera at 14:00 and 5:30, respectively. Multispectral images were taken between 10:00 and 14:00 to calculate soil α [38]:

$$\alpha = 0.606\rho_{band,1} + 0.286\rho_{band,2} + 0.244\rho_{band,3} + 0.164\rho_{band,4} \quad (11)$$

where $\rho_{band,1}$, $\rho_{band,2}$, $\rho_{band,3}$, and $\rho_{band,4}$ are the reflectivity in the blue (459–491 nm), green (546–573 nm), red (660–676 nm) and near-infrared (814–871 nm) bands, respectively.



Figure 2. (a) DJI M300 RTK, (b) Zenmuse H20T thermal infrared camera, (c) RedEdge-MX five-channel multispectral camera, (d) temperature logger, (e) SP-110 solar total radiation sensor.

The total solar radiation intensity in the ATI-R index was obtained by a total radiation sensor (SP-110, Apogee Instruments, Inc., Logan, UT, USA, Figure 2e) placed on a fixed platform located 2 m above the ground surface. The spectral of SP-110 ranges from 360 to 1120 nm with 0.2 mV per $\text{W}\cdot\text{m}^{-2}$ of sensitivity. The sensor records the half-hourly average solar irradiance value, and the cumulative total solar radiation intensity is the integration of irradiance over time.

$$R_t = (I_{0600} + I_{0630} + \dots + I_{1400}) \cdot t \cdot S \quad (12)$$

where I_{0600} , I_{0630} , \dots , I_{1400} are the mean values of irradiance ($\text{W}\cdot\text{m}^{-2}$) from 5:30 to 6:00, 6:00 to 6:30, \dots , and 13:30 to 14:00, respectively. t is the measurement time of the sensor, which is 30 min in this study, and S is the area of soil that receives solar radiation, taken as 1 m^2 in this study.

Three sampling points were randomly marked within the square area ($1.5 \text{ m} \times 1.5 \text{ m}$) in the center of each plot, soils at 0–5 cm were sampled and the oven-drying method was then performed to determine the VWC. Meanwhile, ΔT and α were obtained from thermal infrared images (Equation (10)) and multispectral images (Equation (11)) at posi-

tions corresponding to the marked sampling points to calculate the ATI-R index and ATI index, respectively.

Watering occurred on May 1st and May 6th during the experiment, and rainfall occurred on May 5th and 9th, so we did not conduct the sampling described above on those days.

2.3. Methods Evaluation

The R^2 was calculated to analyze the correlation between the ATI-R/ATI index and the VWC. The RMSE and mean absolute error (MAE) were calculated to evaluate the performance of the ATI-R/ATI method for VWC measurement.

$$R^2 = \frac{\sum(VWC_{cal} - VWC_{mean})^2}{\sum(VWC_{oven} - VWC_{mean})^2} \quad (13)$$

$$RMSE = \sqrt{\frac{\sum(VWC_{cal} - VWC_{oven})^2}{n}} \quad (14)$$

$$MAE = \frac{1}{n} \sum |VWC_{oven} - VWC_{cal}| \quad (15)$$

where VWC_{cal} , VWC_{oven} , and VWC_{mean} are the VWC calculated by the ATI-R/ATI method, the VWC measured by the oven-drying method, and the mean value of VWC_{oven} , respectively.

3. Results and Discussion

3.1. Statistics of the Experimental Data

3.1.1. Weather

Figure 3 shows air temperature and total solar irradiance results. The air temperature and total solar irradiance generally increased during each warming process (5:30–14:00). On May 2nd, May 3rd, and May 4th, the air temperature increased to a maximum value of approximately 33 °C (Figure 3a), the solar irradiance increased to approximately 900 $W \cdot m^{-2}$ (Figure 3b), and the cumulative solar radiation intensity was higher than 17.4 MJ (Figure 3c). The temperature and solar radiation variations were similar during the warming processes on May 2nd, 3rd, and 4th. On May 7th and May 11th, the air temperature increased gradually to a maximum of approximately 20 °C, while the variations in the solar radiation differed, fluctuating approximately 750 $W \cdot m^{-2}$ on May 7th and approximately 350 $W \cdot m^{-2}$ on May 11th. On May 8th, the air temperature remained at approximately 13 °C without significant changes, and the solar irradiance only fluctuated at approximately 200 $W \cdot m^{-2}$.

The six heating processes were divided into three weather types: sunny (May 2nd, May 3rd, May 4th), cloudy (May 7th and May 11th), and overcast (May 8th), based on temperature, solar irradiance, and cumulative solar radiation intensity variations. Sunny days were when the temperature and solar irradiance increased significantly with time, and the cumulative solar radiation intensity was higher than 15 MJ. Cloudy days were when the temperature and solar irradiance increased gradually, and the cumulative solar radiation intensity was 6–15 MJ. An overcast day was when the temperature and irradiance increased non-significantly, and the cumulative radiation intensity was lower than 6 MJ.

3.1.2. Soil VWC and Temperature

Figure 4a shows the soil VWCs under different moisture treatments. On the day after watering (May 2nd and 7th), the VWC difference among treatments was approximately 0.03 $cm^3 \cdot cm^{-3}$, consistent with the experimental design. On May 4th, the VWC under the T0 treatment was $0.11 \pm 0.01 cm^3 \cdot cm^{-3}$, whereas the VWC under the T0 treatment was $0.14 \pm 0.02 cm^3 \cdot cm^{-3}$ on May 7th due to rainfall that occurred on May 5th. A similar impact on the VWC from a rain event also occurred on May 9th.

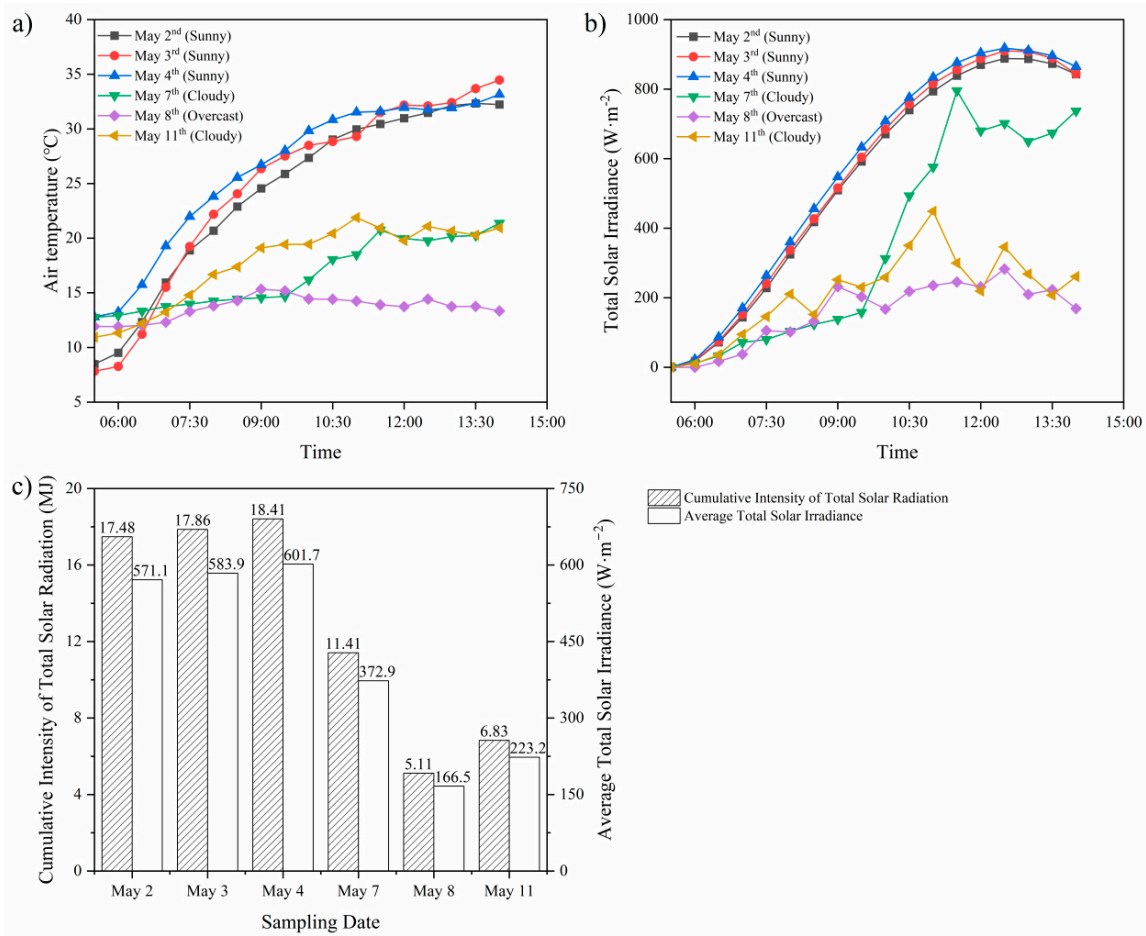


Figure 3. (a) Air temperature, (b) total solar irradiance, and (c) cumulative total solar radiation intensity and average solar total irradiance during heating processes (5:30–14:00) on sunny days (May 2nd, May 3rd, and May 4th), cloudy days (May 7th and May 11th), and overcast days (May 8th).

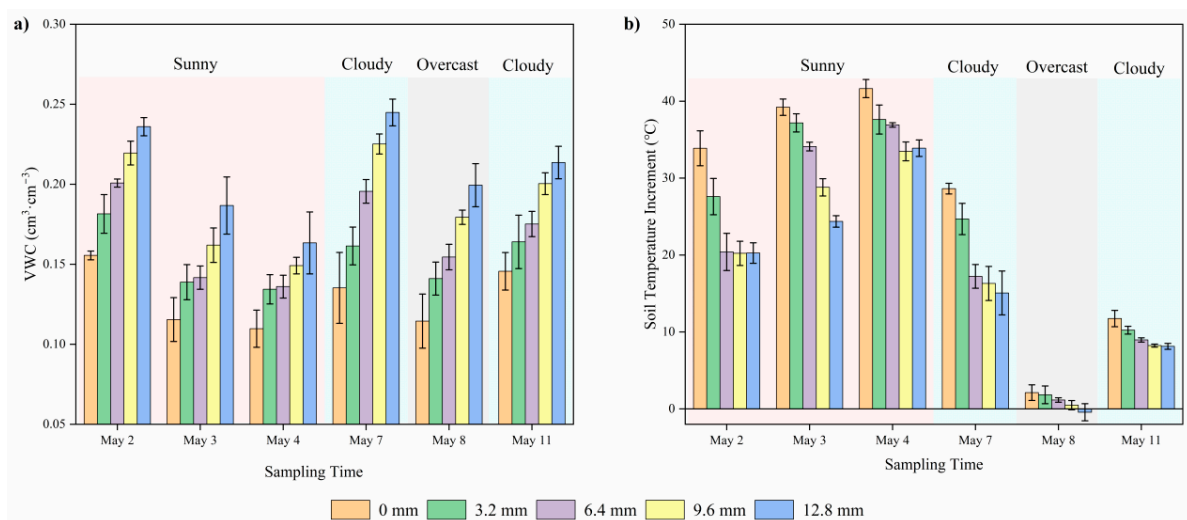


Figure 4. (a) Soil VWCs in 0, 3.2, 6.4, 9.6, and 12.8 mm water treatments, and (b) the soil temperature increments under the heating processes during sunny days (May 2nd, 3rd, and 4th), cloudy days (May 7th and 11th), and the overcast day (May 8th).

Figure 4b shows the soil temperature increments under each treatment during six heating processes. On sunny days, the soil temperature increment is approximately 20–40 °C,

and the lower the VWC is, the higher the temperature increment. On cloudy days, the soil temperature increment decreased to 9–29 °C. On the overcast day, the temperature increment was only 3 °C, or was even a negative value.

The above results indicate that the solar radiation intensity also affects the soil temperature difference besides the VWC. The effect of the VWC on the soil temperature increments is significant when the solar radiation intensity is higher and is less significant when the energy input is lower [39]. For example, on May 3rd (sunny, R_t was 17.86 MJ), the maximum difference in VWC was $0.08 \text{ cm}^3 \cdot \text{cm}^{-3}$, and the maximum difference in the soil temperature increment was 15 °C. On May 11 (cloudy, R_t was 6.83 MJ), the maximum difference in the VWC was $0.07 \text{ cm}^3 \cdot \text{cm}^{-3}$, and the maximum difference in the temperature increment was only 3 °C. Therefore, it is necessary to clarify the solar radiation intensity that causes the soil temperature increment.

3.2. Comparison of the ATI-R and ATI Methods

The correlations between the ATI-R method and VWC and the ATI method and VWC are shown and discussed separately in three ways: (a) with data from a single heating process; (b) with data from multiple heating processes under the same weather type; and (c) with data from multiple heating processes of inconsistent weather types.

3.2.1. Single Heating Process

The correlations between ATI-R and VWC, and ATI and VWC during each heating process were calculated, and the results are shown in Table 1.

Table 1. Linear regression results between ATI/ATI-R and VWC under a single heating process.

Date	Weather Condition	ATI-R		ATI	
		Linear Regression Equation	R ²	Linear Regression Equation	R ²
May 2nd	Sunny	$y = 0.0002x + 0.1183$	0.724	$y = 3.0367x + 0.1183$	0.724
May 3rd	Sunny	$y = 0.0003x + 0.0503$	0.723	$y = 5.8457x + 0.0503$	0.723
May 4th	Sunny	$y = 0.0005x - 0.0066$	0.722	$y = 9.9669x - 0.0066$	0.722
May 7th	Cloudy	$y = 0.0003x + 0.1018$	0.797	$y = 3.1495x + 0.1018$	0.797
May 8th	Overcast	$y = -2 \times 10^{-7}x + 0.1579$	0.027	$y = -0.0015x + 0.1579$	0.027
May 11th	Cloudy	$y = 0.0002x + 0.0859$	0.756	$y = 1.527x + 0.0859$	0.756

The R² from the linear regression showed that ATI-R and ATI correlated well with VWC under single sunny and cloudy days, with R² above 0.700. However, both the ATI-R and ATI methods failed on an overcast day. The reason is that the solar radiation intensity was weak on May 8th ($R_t = 5.11 \text{ MJ}$, Figure 3c) and caused the soil temperature increment to be low or negative (ΔT ranged from -1.5 to 3 °C , Figure 4b). The ΔT is a denominator in the ATI-R and ATI indices (Equations (1) and (8)). Low or negative values of ΔT make the indices extremely large or small, thus weakening the correlation.

Observation of the linear regression equations of the two methods with VWC revealed that the slopes of the equations for the ATI-R method were similar for the different heating processes (except for May 8, which was cloudy). In contrast, the slopes for the ATI method varied considerably. This could lead to the ATI-VWC equations obtained using a single heating process as the dataset, applied to other heating processes, to produce significant errors. The ATI-VWC and ATI-R-VWC linear regression equations for each day were used as predictive models to confirm this assumption. The models were validated with the remaining five heating processes as validation datasets. The results are shown in Figure 5. The dates in the horizontal coordinate indicate that the data of the day was used as the modeling set, and the dates in the vertical coordinate indicate that the data of the day was used as the validation set.

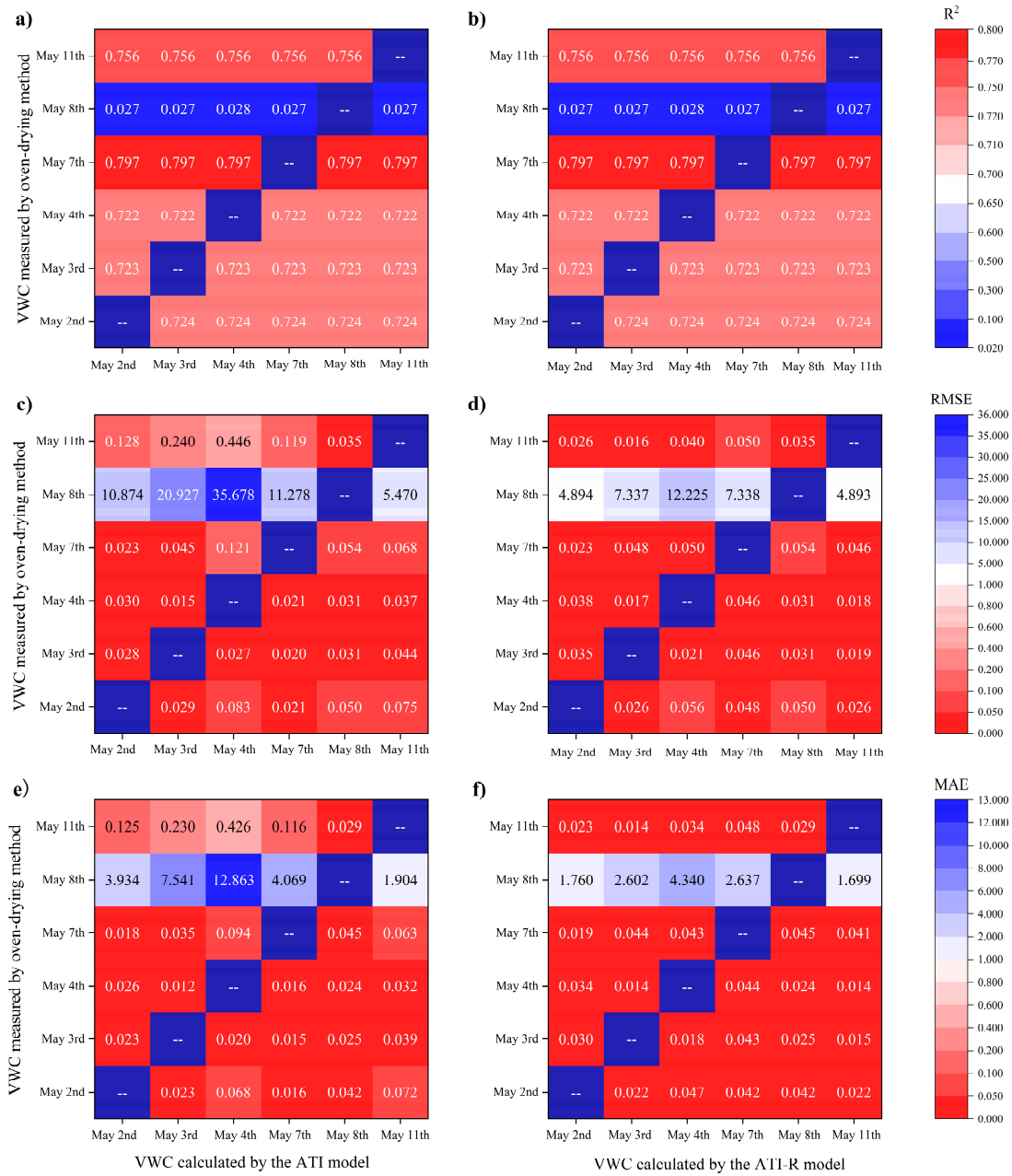


Figure 5. (a) R^2 of ATI method validation results with ATI-VWC for a single heating process as the modeling set, (b) R^2 of ATI-R method validation results with ATI-R-VWC for a single heating process as the modeling set, (c) RMSE of ATI method validation results with ATI for a single heating process as the modeling set, (d) RMSE of ATI-R method validation results with ATI-R for a single heating process as the modeling set, (e) MAE of ATI method validation results with ATI for a single heating process as the modeling set, and (f) MAE of ATI-R method validation results with ATI-R for a single heating process as the modeling set.

Figure 5a,b show the R^2 between the VWC estimated by the ATI and ATI-R methods and the measured VWC, respectively. It was found that the R^2 of both methods was above 0.70 except for the overcast day, indicating good correlations between the two methods and the VWC on both sunny and cloudy days. At the corresponding positions in Figure 5a,b, the R^2 were the same for both methods. Because ATI-R is ATI multiplied by R_t , and R_t is equivalent to a constant during a single heating process. This can also be seen in the equations in Table 1, where the two equations for the same day differ only in slope.

To further compare the performance of the two methods, the RMSE and MAE of the two methods are presented in Figure 5c–f, respectively. The ATI method was similar to the ATI-R method in its effectiveness in estimating VWC on sunny days using sunny day data as a predictive model (called the sunny-day model). When predicting VWC on cloudy days with the sunny-day model, the ATI method exhibited more significant bias, with $RMSE_{ATI} > 0.100 \text{ cm}^3 \cdot \text{cm}^{-3}$ and $RMSE_{ATI-R} \leq 0.050 \text{ cm}^3 \cdot \text{cm}^{-3}$, and with $MAE_{ATI} > 0.090 \text{ cm}^3 \cdot \text{cm}^{-3}$ and $MAE_{ATI-R} < 0.050 \text{ cm}^3 \cdot \text{cm}^{-3}$. Both methods showed some bias when predicting VWC on sunny days with the cloudy-day model, with $RMSE_{ATI-R} \leq 0.050 \text{ cm}^3 \cdot \text{cm}^{-3}$ and $MAE_{ATI-R} < 0.050 \text{ cm}^3 \cdot \text{cm}^{-3}$, while $RMSE_{ATI}$ and MAE_{ATI} were above $0.050 \text{ cm}^3 \cdot \text{cm}^{-3}$ in some validation sets. The ATI model for May 7th predicted better than ATI-R with VWC on sunny days, probably because of the higher radiation and lower temperature variation on May 7th, which made the soil temperature change a lower amount during the prescribed warming; thus the ATI-R index overestimated VWC on this day.

In addition, the ATI showed a good correlation with the VWC on cloudy days, which differed from the clear and cloudless conditions suggested by existing studies [30]. This phenomenon is because in this study, the soil temperature still increased on cloudy days (May 7th: 13–29 °C; and May 11th: 8–12 °C). Additionally, the multispectral images used to calculate albedo were acquired when the weather conditions were stable, ensuring consistency among images during the same sampling processes [40]. The effect of clouds can be approximated to be the same on soil spectral information because the UAV flies under clouds.

The results above indicate that ATI and ATI-R methods correlated with VWC for a single heating process on sunny and cloudy days. However, both methods failed on overcast days when soil heating was insignificant or negative. Moreover, when weather conditions for relationship exploration were different (radiation differences), the ATI method produced a more significant bias in estimating the VWC for different weather conditions than the ATI-R method.

3.2.2. Multiple Heating Processes under the Same Weather Type

We compared the performance of the ATI-R and ATI methods for the VWC measurement under the same weather type: sunny (May 2nd, May 3rd, and May 4th), cloudy (May 7th and May 11th). Since the ATI-R and ATI methods failed on the overcast day, the overcast data (May 8th) were not repeated in this subsection. The results are shown in Figure 6.

Figure 6a,b show the correlation between ATI-R and VWC and the correlation between ATI and VWC under sunny conditions, respectively. The ATI-R and ATI correlated well with the VWC, with $R^2_{ATI-R} = 0.775$, $RMSE_{ATI-R} = 0.023 \text{ cm}^3 \cdot \text{cm}^{-3}$, and $MAE_{ATI-R} = 0.018 \text{ cm}^3 \cdot \text{cm}^{-3}$ (Figure 6a), and $R^2_{ATI} = 0.778$, $RMSE_{ATI} = 0.018 \text{ cm}^3 \cdot \text{cm}^{-3}$, and $MAE_{ATI} = 0.013 \text{ cm}^3 \cdot \text{cm}^{-3}$ (Figure 6b), respectively. Under cloudy conditions, $R^2_{ATI-R} = 0.565$, $RMSE_{ATI-R} = 0.024 \text{ cm}^3 \cdot \text{cm}^{-3}$ and $MAE_{ATI-R} = 0.020 \text{ cm}^3 \cdot \text{cm}^{-3}$ (Figure 6c), and $R^2_{ATI} = 0.156$, $RMSE_{ATI} = 0.033 \text{ cm}^3 \cdot \text{cm}^{-3}$ and $MAE_{ATI} = 0.027 \text{ cm}^3 \cdot \text{cm}^{-3}$ (Figure 6d), indicating that the ATI-R method correlated better with the VWC than the ATI method correlated with the VWC (Figure 6c,d).

The results under the same weather type show that the ATI-R and ATI methods had acceptable and similar performances on sunny days; the ATI-R method outperformed the ATI method on the cloudy days. On sunny days, the ATI-R and ATI methods similarly performed well because the cumulative radiation intensities during the three warming processes were similar ($R_{t-May2} = 17.48 \text{ MJ}$, $R_{t-May3} = 17.86 \text{ MJ}$, $R_{t-May4} = 18.41 \text{ MJ}$), and the daily differences in the solar radiation were slight (ΔR_t ranged from 0.38–0.93 MJ). Such weather was also consistent with clear and cloudless conditions suitable for the ATI method [30]. On cloudy days, the daily variations in solar radiation were significant and unignorable (ΔR_t was 4.58 MJ), resulting in the different performances of the ATI-R and

ATI methods. However, since the ATI-R method adds the solar radiation measurement to identify the variations in R_t , the ATI-R method outperforms the ATI method on cloudy days.

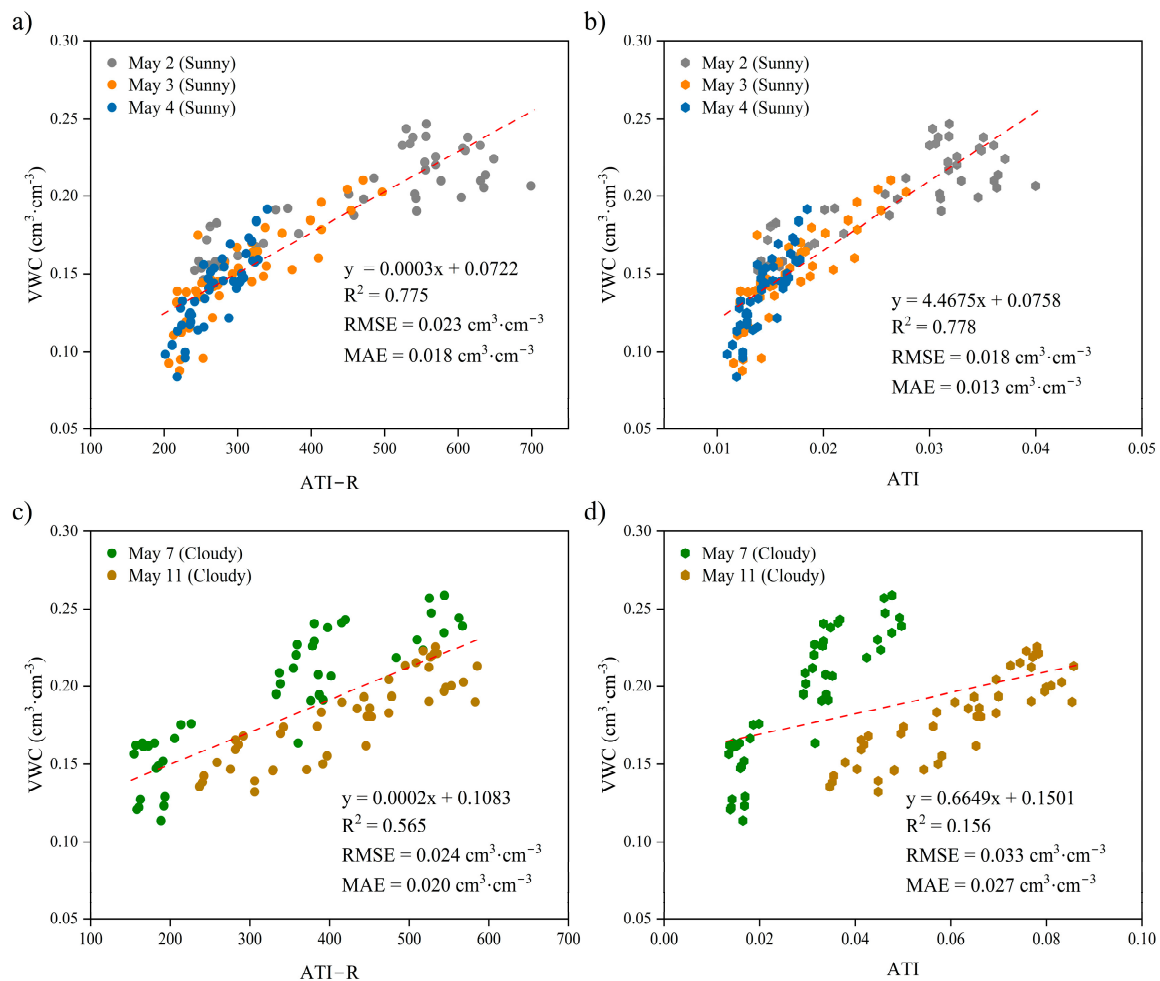


Figure 6. (a) Correlation between the ATI-R and the VWC on sunny days, (b) correlation between the ATI and the VWC on sunny days, (c) correlation between the ATI-R and the VWC on cloudy days, (d) correlation between the ATI and the VWC on cloudy days. The red-dashed line is the result of the linear fit.

Similar to Section 3.2.1, the sunny-day dataset was used to model and predict VWC for cloudy days, and the cloudy-day dataset was used to model and predict VWC for sunny days. The results are displayed in Table 2.

Table 2. Estimated results of VWC under different weather conditions by ATI-R and ATI methods.

Modeling Set	ATI-R			ATI		
	R ²	RMSE (cm ³ ·cm ⁻³)	MAE (cm ³ ·cm ⁻³)	R ²	RMSE (cm ³ ·cm ⁻³)	MAE (cm ³ ·cm ⁻³)
Sunny-day dataset	0.565	0.027	0.022	0.156	0.127	0.096
Cloudy-day dataset	0.775	0.025	0.020	0.778	0.035	0.029

The first row of the data indicates that the ATI-R-VWC model was established with the sunny-day dataset, and the ATI-R of the cloudy-day dataset was brought into the model to calculate a set of VWC estimates. R², RMSE, and MAE between VWC estimates and measured VWC are calculated and used for method evaluation.

Table 2 shows that although the correlations between the ATI-R and ATI methods with VWC under sunny conditions are similar, the two methods appear significantly different when used to estimate VWC under cloudy conditions. Similar results are seen in the

estimation of sunny-day VWC with the cloudy-day models. The above results show that the ATI-R method can be used to estimate the VWC under different weather conditions with higher accuracy than the ATI method.

3.2.3. Multiple Heating Processes under Different Weather Types

The ATI-R and ATI methods were compared under inconsistent weather types. Inconsistent weather included (a) a combination of sunny and cloudy days (May 2nd, 3rd, 4th, 7th, and 11th), (b) a combination of cloudy and overcast days (May 7th, May 11th, and May 8th), and (c) a combination of sunny and overcast days (May 2nd, 3rd, 4th, and 8th).

Figure 7 illustrates the correlation between ATI-R with VWC and the correlation between ATI with VWC under the two-by-two combinations of the three types of weather. On combined sunny and cloudy days, the ATI-R method correlated better with the VWC than the ATI method did, where $R^2_{\text{ATI-R}} = 0.67$, $\text{RMSE}_{\text{ATI-R}} = 0.028 \text{ cm}^3 \cdot \text{cm}^{-3}$, $\text{MAE}_{\text{ATI-R}} = 0.018 \text{ cm}^3 \cdot \text{cm}^{-3}$, and $R^2_{\text{ATI}} = 0.31$, $\text{RMSE}_{\text{ATI}} = 0.032 \text{ cm}^3 \cdot \text{cm}^{-3}$, $\text{MAE}_{\text{ATI}} = 0.025 \text{ cm}^3 \cdot \text{cm}^{-3}$ (Figure 7a,b). However, after considering data from the overcast day, neither the ATI-R method nor the ATI index showed correlations with VWC (R^2 lower than 0.01, Figure 7c–f). In addition, vertical lines were found in Figure 7c–f due to the data for the overcast day deviating significantly from those for sunny and cloudy days. The purple dots indicate data from the overcast day, representing ATI-R ranging from $-17,000$ to $17,000$ and ATI ranging from -2.5 to 2.5 , respectively. In contrast, the points in Figure 7a,b were from data from sunny and cloudy days; ATI-R ranged from 150 to 700, and ATI ranged from 0.015 to 0.085.

The results under inconsistent weather types showed a good correlation between the ATI-R method and VWC as long as there were significant increases in soil temperature, even if different weather types were mixed in the dataset. The more complex solar radiation intensity under inconsistent weather types (6.84–18.41 MJ), compared to the same weather type (17.84–18.41 MJ), led to daily variations that could not be approximated equally in solar radiation. The lack of radiation measurements made it difficult for the ATI method to explain the conditions under which the soil temperature varied. Therefore, the correlation between the ATI index and VWC was weak under inconsistent weather types. However, both methods failed when introducing data from the overcast day, indicating that the ATI-R/ATI index of the corresponding processes is hardly correlated with the VWC when there is no significant increase in soil temperature ($\Delta T < 3 \text{ }^\circ\text{C}$, in this study, Figure 4b) and that the overcast days should not be considered in the multiple soil-heating processes.

In this study, the ATI-R method expands the applicability of the ATI method by adding the total solar radiation measurement and calculating the cumulative solar radiation intensity of the soil-heating process. The ATI-R method was applied to multiple soil-heating processes with significant increases in soil temperature ($\Delta T \geq 7 \text{ }^\circ\text{C}$) even if these processes had substantial differences in solar radiation intensity. The R_t of the ATI-R method that was applicable to multiple processes ranged from 6.84 to 18.41 MJ, and the half-hourly mean irradiance ranged from 223.2 to $601.7 \text{ W} \cdot \text{m}^{-2}$. In contrast, the ATI method is only applicable to multiple soil-heating processes with similar radiation intensities. The difference in the R_t of the ATI method applicable for multiple processes was small at 0.93 MJ (17.48–18.41 MJ), while the correlation between the ATI method and the VWC was weak when the difference in R_t was 4.58 MJ (6.83–11.41 MJ), with $R^2_{\text{ATI}} = 0.156$ and $\text{RMSE}_{\text{ATI}} = 0.033 \text{ cm}^3 \cdot \text{cm}^{-3}$. These results indicate that adding a solar radiation measurement sensor allows for quantifying the energy input during each soil-heating process. The energy input from the sun varies in different processes, which leads to different ΔT values for different heating processes, even for soils with the same VWC. Although α can represent the proportion of energy absorbed by the soil [28,41], the actual energy input that causes the soil temperature variation, especially for multiple processes, cannot be replaced by α . Therefore, quantifying the solar radiation intensity during different warming processes is necessary, which makes data from different processes comparable.

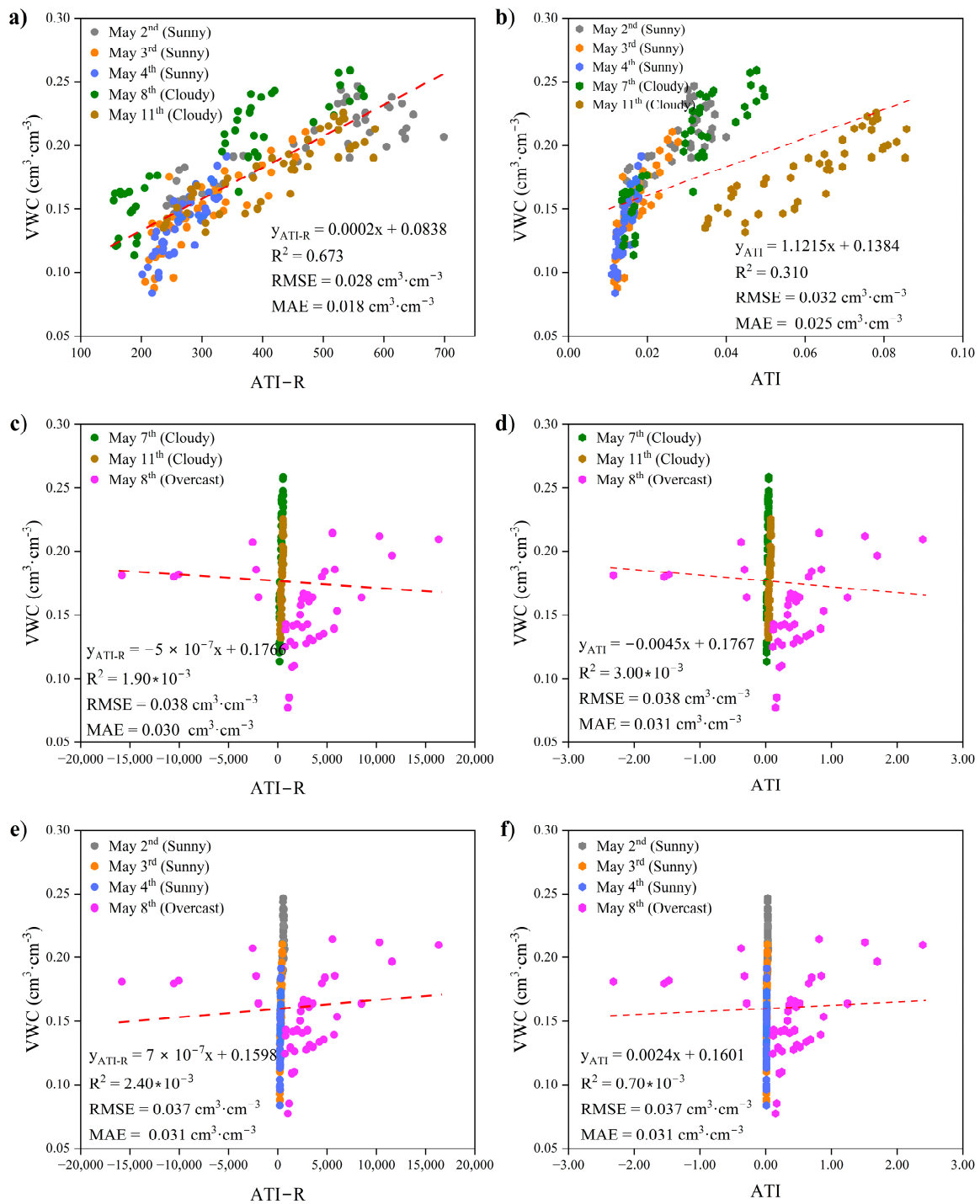


Figure 7. (a) Correlation between the ATI-R method and the VWC on sunny and cloudy days, (b) correlation between the ATI method and the VWC on sunny and cloudy days, (c) correlation between the ATI-R method and the VWC on cloudy and overcast days, (d) correlation between the ATI method and the VWC on cloudy and overcast days, (e) correlation between the ATI-R method and the VWC on sunny and overcast days, and (f) correlation between the ATI method and the VWC on sunny and overcast days. The red-dashed line is the result of the linear fit.

In this study, adding a total solar radiation sensor increases the monitoring cost, which is acceptable because it extends the applicability of the traditional ATI method and improves the accuracy of soil moisture monitoring in multiple processes. Meanwhile, this study was carried out in an agricultural field of flat terrain, where the size of the experimental area

matched the effective measurement scale represented by the solar radiation sensor and where factors such as the terrain caused less variation among the plots [42]. Therefore, the ATI-R method proposed in this study is suitable for long-term soil moisture monitoring at the farm-scale in plains areas. With the increase in the monitoring area, a single radiation sensor cannot accurately represent the solar radiation in the study area, and the number of sensors needs to be increased, which undoubtedly will increase the monitoring cost and introduce some errors.

Additionally, the use of the flexible and convenient UAV platform can better meet the needs of the ATI-R method, which is also one of the factors in improving the accuracy of soil moisture measurement. The ATI-R method must obtain the soil temperature at the beginning and end of a specific soil-heating process to calculate the soil temperature increment. The UAV-carried thermal infrared camera can capture the infrared soil image at the corresponding time required to obtain the soil temperature [43]. As a result, the soil temperature information obtained by the UAV and the solar radiation information obtained by the radiation sensor are highly temporally matched, making the ATI-R index calculation more accurate. Soil albedo is another critical parameter used to calculate the ATI-R index. In this study, to ensure the accuracy of the α calculation, UAV-based multispectral images were obtained under stable weather conditions such as cloud cover and wind speed [44]. Relatively stable weather conditions can ensure comparability between α in the same sampling process, and a flexible UAV platform can meet this sampling requirement. Furthermore, resampling can occur even if weather conditions change significantly during sampling, since the UAV-based visible-near-infrared (VNIR) images and thermal infrared (TIR) images are all surface measurements. Therefore, we validate the method on bare soil, which is more intuitive and accurate to reflect the correlation between soil temperature and moisture. In the future, if vegetation needs to be considered, the ATI-R method can extract soil pixels by supervised classification before modeling under low-vegetation cover [45]. In contrast, the ATI-R method may also be limited under medium and high-vegetation cover due to the lack of a physically meaningful and clear vegetation canopy–land surface temperature conversion relationship.

4. Conclusions

This study proposed an ATI-R method for soil moisture estimation under multiple processes with different weather conditions based on thermal infrared UAV-based remote sensing. The ATI-R method quantifies the surface energy input during different soil-heating processes by adding solar radiation measurement during the heating processes. A moisture control experiment was designed in flat topographic farmland in Henan Province, China. The performance of the ATI-R method for VWC estimation was verified by comparing the ATI method. The main findings are as follows:

- (1) ATI-R and ATI methods both had acceptable correlations with VWC during single heating process. However, using the single-day expression, the ATI-R was more accurate in estimating VWC under conditions of significant differences in solar radiation. Both methods failed on cloudy days with insignificant soil heating.
- (2) Under multiple heating processes with similar weather, ATI-R and ATI correlated well with VWC on sunny days with similar solar radiation. At the same time, ATI-R correlated better with VWC on cloudy days with differences in solar radiation than ATI. ATI-R obtained more accurate estimates when estimating VWC on cloudy days with a model with sunny-day data.
- (3) The correlation between ATI-R and VWC was significantly better than that between ATI and VWC when the combination of sunny and cloudy days was considered. In contrast, the correlation between the two methods and VWC was almost zero, as long as cloudy days with insignificant surface heating ($\Delta T \leq 3$ °C, in this study, Figure 4b) were considered.

Comparison results of the ATI-R method with the ATI method showed that the ATI-R method incorporating solar radiation measurements broadened the weather applicability conditions of the method and improved the accuracy of multi-process VWC measurements. Moreover, the ATI-R method can be used to estimate VWC under different weather conditions (except overcast), which provides a new idea for farm-scale soil moisture monitoring. The ATI-R method is currently only aimed at VWC measurements on bare soil in plains. Although the possibility of applying it to low-vegetation cover scenarios is suggested, more consideration should be given to VWC monitoring in vegetated areas, including medium- and high-vegetation cover.

Author Contributions: Conceptualization, R.J., X.L. and J.L.; methodology, R.J., X.L. and J.L.; software, R.J., Y.N., J.J. and B.M.; validation, R.J. and Y.N.; investigation, R.J., Y.J., K.X. and C.W.; resources, R.J., Y.J. and K.X.; data curation, R.J.; writing—original draft preparation, R.J.; writing—review and editing, R.J., J.L. and X.L.; supervision, J.L., J.Z. and X.L.; funding acquisition, J.L. and X.L. All authors have read and agreed to the published version of the manuscript.

Funding: The National Key Research and Development Program of China (Funding number, 2022YFD1500502), the Innovation Program of ISSAS (grant No. ISSASIP2207), the Strategic Priority Research Program of the Chinese Academy of Sciences (grant No. XDA28010401).

Data Availability Statement: The data presented in this study are available on request from the corresponding author.

Acknowledgments: We would like to express our appreciation to the Fengqiu State Key ArgoEcological Experimental Station for providing the experimental site support for this research.

Conflicts of Interest: The authors declare no conflict of interest.

References

1. Yuan, L.; Li, L.; Zhang, T.; Chen, L.; Zhao, J.; Hu, S.; Cheng, L.; Liu, W. Soil Moisture Estimation for the Chinese Loess Plateau Using MODIS-derived ATI and TVDI. *Remote Sens.* **2020**, *12*, 3040. [[CrossRef](#)]
2. Cheng, M.; Jiao, X.; Liu, Y.; Shao, M.; Yu, X.; Bai, Y.; Wang, Z.; Wang, S.; Tuohuti, N.; Liu, S.; et al. Estimation of soil moisture content under high maize canopy coverage from UAV multimodal data and machine learning. *Agric. Water Manag.* **2022**, *264*, 107530. [[CrossRef](#)]
3. Bian, J.; Zhang, Z.; Chen, J.; Chen, H.; Cui, C.; Li, X.; Chen, S.; Fu, Q. Simplified Evaluation of Cotton Water Stress Using High Resolution Unmanned Aerial Vehicle Thermal Imagery. *Remote Sens.* **2019**, *11*, 267. [[CrossRef](#)]
4. Ezenne, G.I.; Jupp, L.; Mantel, S.K.; Tanner, J.L. Current and potential capabilities of UAS for crop water productivity in precision agriculture. *Agric. Water Manag.* **2019**, *218*, 158–164. [[CrossRef](#)]
5. Crusiol, T.G.L.; Nanni, R.M.; Furlanetto, H.R.; Sibaldelli, R.N.R.; Cezar, E.; Mertz-Henning, M.L.; Nepomuceno, L.A.; Neumaier, N.; Farias, B.R.J. UAV-based thermal imaging in the assessment of water status of soybean plants. *Int. J. Remote Sens.* **2020**, *41*, 3243–3265. [[CrossRef](#)]
6. Lu, F.; Sun, Y.; Hou, F. Using UAV Visible Images to Estimate the Soil Moisture of Steppe. *Water* **2020**, *12*, 2334. [[CrossRef](#)]
7. Bai, X.; Chen, Y.; Chen, J.; Cui, W.; Tai, X.; Zhang, Z.; Cui, J.; Ning, J. Optimal window size selection for spectral information extraction of sampling points from UAV multispectral images for soil moisture content inversion. *Comput. Electron. Agric.* **2021**, *190*, 106456. [[CrossRef](#)]
8. Zhu, S.; Cui, N.; Zhou, J.; Xue, J.; Wang, Z.; Wu, Z.; Wang, M.; Deng, Q. Digital Mapping of Root-Zone Soil Moisture Using UAV-Based Multispectral Data in a Kiwifruit Orchard of Northwest China. *Remote Sens.* **2023**, *15*, 646. [[CrossRef](#)]
9. Wang, L.; Qu, J.J. Satellite remote sensing applications for surface soil moisture monitoring: A review. *Front. Earth Sci. China* **2009**, *3*, 237–247. [[CrossRef](#)]
10. Soliman, A.; Heck, R.; Brenning, A.; Brown, R.; Miller, S. Remote Sensing of Soil Moisture in Vineyards Using Airborne and Ground-Based Thermal Inertia Data. *Remote Sens.* **2013**, *5*, 3729–3748. [[CrossRef](#)]
11. Keshavarz, R.M.; Vazifedoust, M.; Alizadeh, A. Drought monitoring using a Soil Wetness Deficit Index (SWDI) derived from MODIS satellite data. *Agric. Water Manag.* **2014**, *132*, 37–45. [[CrossRef](#)]
12. Ainiwaer, M.; Ding, J.; Kasim, N.; Wang, J.; Wang, J. Regional scale soil moisture content estimation based on multi-source remote sensing parameters. *Int. J. Remote Sens.* **2019**, *41*, 3346–3367. [[CrossRef](#)]
13. Bai, Y.; Zhao, T.; Jia, L.; Cosh, H.M.; Shi, J.; Peng, Z.; Li, X.; Wigneron, J. A multi-temporal and multi-angular approach for systematically retrieving soil moisture and vegetation optical depth from SMOS data. *Remote Sens. Environ.* **2022**, *280*, 113190. [[CrossRef](#)]

14. Hu, F.; Wei, Z.; Yang, X.; Xie, W.; Li, Y.; Cui, C.; Yang, B.; Tao, C.; Zhang, W.; Meng, L. Assessment of SMAP and SMOS soil moisture products using triple collocation method over Inner Mongolia. *J. Hydrol. Reg. Stud.* **2022**, *40*, 101027. [[CrossRef](#)]
15. Roberts, T.M.; Colwell, I.; Chew, C.; Lowe, S.; Shah, R. A Deep-Learning Approach to Soil Moisture Estimation with GNSS-R. *Remote Sens.* **2022**, *14*, 3299. [[CrossRef](#)]
16. Sinha, A.K. Variations in soil spectral reflectance related to soil moisture, organic matter and particle size. *J. Indian Soc. Remote Sens.* **1987**, *15*, 7–11. [[CrossRef](#)]
17. Shi, J.; Wang, J. Estimation of bare surface soil moisture and surface roughness parameter using L-band SAR image data. *IEEE Trans. Geosci. Remote Sens.* **1997**, *35*, 1254–1266.
18. Munoz-Martin, J.F.; Onrubia, R.; Pascual, D.; Park, H.; Pablos, M.; Camps, A.; Rüdiger, C.; Walker, J.; Monerris, A. Single-Pass Soil Moisture Retrieval Using GNSS-R at L1 and L5 Bands: Results from Airborne Experiment. *Remote Sens.* **2021**, *13*, 797. [[CrossRef](#)]
19. Feldman, A.F.; Chaparro, D.; Entekhabi, D. Error Propagation in Microwave Soil Moisture and Vegetation Optical Depth Retrievals. *IEEE J. Sel. Top. Appl. Earth Obs. Remote Sens.* **2021**, *14*, 11311–11323. [[CrossRef](#)]
20. Ma, C.; Wang, W.; Han, X.; Li, X. Soil Moisture Retrieval in the Heihe River Basin Based on the Real Thermal Inertia Method. *IEEE J. Sel. Top. Appl. Earth Obs. Remote Sens.* **2013**, *6*, 1460–1467. [[CrossRef](#)]
21. Wang, Y.; Peng, J.; Song, X.; Leng, P.; Ralf, L.; Alexander, L. Surface Soil Moisture Retrieval Using Optical/Thermal Infrared Remote Sensing Data. *IEEE Trans. Geosci. Remote Sens.* **2018**, *56*, 5433–5442. [[CrossRef](#)]
22. Liu, Z.; Zhao, L.; Peng, Y.; Wang, G.; Hu, Y. Improving Estimation of Soil Moisture Content Using a Modified Soil Thermal Inertia Model. *Remote Sensing.* **2020**, *12*, 1719. [[CrossRef](#)]
23. Li, C.; Adu, B.; Wu, J.; Qin, G.; Li, H.; Han, Y. Spatial and temporal variations of drought in Sichuan Province from 2001 to 2020 based on modified temperature vegetation dryness index (TVDI). *Ecol. Indic.* **2022**, *141*, 108883. [[CrossRef](#)]
24. Khanal, S.; Fulton, J.; Shearer, S. An overview of current and potential applications of thermal remote sensing in precision agriculture. *Comput. Electron. Agric.* **2017**, *139*, 22–32. [[CrossRef](#)]
25. Messina, G.; Modica, G. Applications of UAV Thermal Imagery in Precision Agriculture State of the Art and Future Research Outlook. *Remote Sens.* **2020**, *12*, 1491. [[CrossRef](#)]
26. Watson, K.; Rowan, L.C.; Offield, T.W. Application of thermal modeling in the geologic interpretation of IR images. *Proc. Seventh Int. Symp. Remote Sens. Environ.* **1971**, *3*, 2017–2041.
27. Pratt, D.A.; Ellyett, C.D. The thermal inertia approach to mapping of soil moisture and geology. *Remote Sens. Environ.* **1979**, *8*, 151–168. [[CrossRef](#)]
28. Price, J.C. On the analysis of thermal infrared imagery: The limited utility of apparent thermal inertia. *Remote Sens. Environ.* **1985**, *18*, 59–73. [[CrossRef](#)]
29. Kahle, B.A. A simple thermal model of the Earth's surface for geologic mapping by remote sensing. *J. Geophys. Res.* **1977**, *82*, 1673–1680. [[CrossRef](#)]
30. Doninck, V.J.; Peters, J.; Baets, D.B.; Clercq, D.M.E.; Ducheyne, E.; Verhoest, E.N. The potential of multitemporal Aqua and Terra MODIS apparent thermal inertia as a soil moisture indicator. *Int. J. Appl. Earth Obs. Geoinf.* **2011**, *13*, 934–941. [[CrossRef](#)]
31. Palombo, A.; Pascucci, S.; Loperte, A.; Lettino, A.; Castaldi, F.; Muolo, M.R.; Santini, F. Soil Moisture Retrieval by Integrating TASI-600 Airborne Thermal Data, WorldView 2 Satellite Data and Field Measurements: Petacciato Case Study. *Sensors* **2019**, *19*, 1515. [[CrossRef](#)] [[PubMed](#)]
32. Sohrabinia, M.; Rack, W.; Zavar-Reza, P. Soil moisture derived using two apparent thermal inertia functions over Canterbury, New Zealand. *J. Appl. Remote Sens.* **2014**, *8*, 083624. [[CrossRef](#)]
33. Song, C.; Jia, L. A Method for Downscaling FengYun-3B Soil Moisture Based on Apparent Thermal Inertia. *Remote Sens.* **2016**, *8*, 703. [[CrossRef](#)]
34. Lu, X.J.; Zhou, B.; Yan, H.B.; Luo, L.; Huang, Y.H.; Wu, C.L. Remote Sensing Retrieval of Soil Moisture in Guangxi Based on Ati and TvdI Models. *ISPRS-Int. Arch. Photogramm. Remote Sens. Spat. Inf. Sci.* **2020**, *XLII-3/W10*, 895–902. [[CrossRef](#)]
35. Kluitenberg, J.G. 5.2 Heat Capacity and Specific Heat. In *Methods of Soil Analysis*; The Soil Science Society of America, Inc.: Madison, WI, USA, 2002; pp. 1201–1208.
36. Abu-Hamdeh, H.N. Thermal Properties of Soils as affected by Density and Water Content. *Biosyst. Eng.* **2003**, *86*, 97–102. [[CrossRef](#)]
37. Campbell, G.S. *Soil Physics with BASIC: Transport Models for Soil-Plant Systems*; Washington State University: Pullman, WA, USA, 1985.
38. Lei, S.; Bian, Z.; Daniels, J.L.; Liu, D. Improved spatial resolution in soil moisture retrieval at arid mining area using apparent thermal inertia. *Trans. Nonferrous Met. Soc. China* **2014**, *24*, 1866–1873. [[CrossRef](#)]
39. Illston, B.G.; Fiebrich, C.A. Horizontal and vertical variability of observed soil temperatures. *Geosci. Data J.* **2017**, *4*, 40–46. [[CrossRef](#)]
40. Sepulcre-Cantó, G.; Zarco-Tejada, P.J.; Jiménez-Muñoz, J.C.; Sobrino, J.A.; Miguel, E.D.; Villalobos, F.J. Detection of water stress in an olive orchard with thermal remote sensing imagery. *Agric. For. Meteorol.* **2006**, *136*, 31–44. [[CrossRef](#)]
41. Price, J.C. Thermal inertia mapping: A new view of the Earth. *J. Geophys. Res.* **1977**, *82*, 2582–2590. [[CrossRef](#)]
42. Perz, R.; Wronowski, K. UAV application for precision agriculture. *Aircr. Eng. Aerosp. Technol.* **2019**, *91*, 257–263. [[CrossRef](#)]
43. Delavarpour, N.; Koparan, C.; Nowatzki, J.; Bajwa, S.; Sun, X. A Technical Study on UAV Characteristics for Precision Agriculture Applications and Associated Practical Challenges. *Remote Sens.* **2021**, *13*, 1204. [[CrossRef](#)]

44. Jiménez-Berni, A.J.; Zarco-Tejada, J.P.; Suárez, L.; Fereres, E. Thermal and Narrowband Multispectral Remote Sensing for Vegetation Monitoring from an Unmanned Aerial Vehicle. *IEEE Trans. Geosci. Remote Sens.* **2009**, *47*, 722–738. [[CrossRef](#)]
45. Zahraa, A.; Sabah, H.J. Accuracy assessment of supervised classification methods for extraction land use maps using remote sensing and GIS techniques. *IOP Conf. Ser. Mater. Sci. Eng.* **2020**, *745*, 012166.

Disclaimer/Publisher’s Note: The statements, opinions and data contained in all publications are solely those of the individual author(s) and contributor(s) and not of MDPI and/or the editor(s). MDPI and/or the editor(s) disclaim responsibility for any injury to people or property resulting from any ideas, methods, instructions or products referred to in the content.